Intense anomalous high harmonics in graphene quantum dots caused by disorder or vacancies

H. K. Avetissian , G. A. Musayelyan, and G. F. Mkrtchian [*]

Centre of Strong Fields Physics at Research Institute of Physics, Yerevan State University, Yerevan 0025, Armenia

This article aims to study the linear and nonlinear optical response of inversion symmetric graphene quantum dots (GQDs) in the presence of on-site disorder or vacancies. The presence of disorder or vacancy breaks the special inversion symmetry, leading to the emergence of intense Hall-type anomalous harmonics. This phenomenon is attributed to the intrinsic time-reversal symmetry breaking in quantum dots with a pseudo-relativistic Hamiltonian, even in the absence of an external magnetic field. We demonstrate that the effects induced by disorder or vacancy have a distinct impact on the optical response of GQDs. In the linear response we observe significant Hall conductivity. In the presence of an intense laser field, we observe the radiation of strong anomalous odd- and even-order harmonics already for relatively small levels of disorder or monovacancy. Both the disorder and vacancy lift the degeneracy of states, thereby creating new channels for interband transitions and enhancing the emission of near-cutoff high-harmonic signals.

I. INTRODUCTION

Theoretical studies of two-dimensional (2D) systems with unique electronic and topological properties can be traced back about 80 years, encompassing areas such as single graphite layers [1,2], zero-gap semiconductors [3], the quantum Hall effect without a magnetic field [4], *d*-wave superconductors [5], and neutrino billiards [6]. However, it was only with the experimental realization of graphene in 2004 [7] that a new frontier in physics opened up: the field of 2D materials featuring pseudo-relativistic charged carriers and nontrivial spatial and band structure topology [8–12]. One remarkable manifestation of the importance of topology is the "mystery of a missing pie" [13] in the DC conductivity of graphene σ_{DC}. Early experiments observed values of σ_{DC} that were π times larger than the predicted value for pristine, disorder-free graphene [14]. Subsequent studies revealed that the value of σ_{DC} strongly depends on various factors, including the boundary conditions of the graphene sheet [15,16], the presence of disorder [17,18], and the interactions among charged carriers [19–21]. This highlighted the intricate interplay between topology, disorder, and carrier interactions in graphene's electrical conductivity.

The optoelectronic properties of graphene undergo significant changes when it is reduced to zero-dimensional structures known as graphene quantum dots (GQDs) [22]. The behavior of GQDs can vary from metallic to insulating, depending on the type of edges they possess [23]. The optical properties of GQDs depend on their size and shape [22,24–27].

Various synthesis methods exist for GQDs, including fragmentation of fullerene molecules [28] and nanoscale cutting of graphite combined with exfoliation [29], decomposition of hydrocarbons [30]. The confinement of electronic states in GQDs has been confirmed through scanning tunneling microscopy measurements [31]. Along with graphene, GQDs have garnered significant attention due to their unique opto-electronic properties and their potential applications in diverse fields such as bioimaging [32,33], photovoltaics [34], quantum computing [35], photodetectors [36], energy storage [37], sensing [38], and metal ion detection [39].

The potential to engineer the energy spectrum and optical transitions of GQDs has drawn significant attention also in the field of strong-field physics [40]. This is due to the promising prospects for GQDs in extreme nonlinear optics applications, including high-order harmonic generation (HHG) [41]. Theoretical studies have predicted strong HHG from fullerenes [42–46], graphene nanoribbons [47–49], and GQDs [50–54]. These studies have also highlighted significant alterations in the nonlinear optical properties by manipulating the size, shape, and edges of these systems. It is worth noting that the electron-electron interactions have been recognized as a crucial factor that influence the optical phenomena in the mentioned nanostructures [54].

In most previous theoretical studies, the interaction of graphenelike systems with the laser fields has been primarily focused on perfect crystal structures with periodic lattices. However, as is known, disorder or point defects in graphene, such as vacancies, can strongly affect the electronic properties of the system, since those defects support quasilocalized electronic states [55–57]. There have been several studies making intriguing predictions that any distortion in the graphene lattice leads to the generation of strong gauge fields [58–60], effectively acting as a pseudo-magnetic field and giving rise to a pseudo-quantum-Hall effect. By applying strain, it is possible to create nearly uniform pseudo-magnetic fields that exceed 10 T [61]. Remarkably, graphene nanobubbles exhibit Landau levels forming in the presence of strain-induced pseudo-magnetic fields greater than 300 T [62].
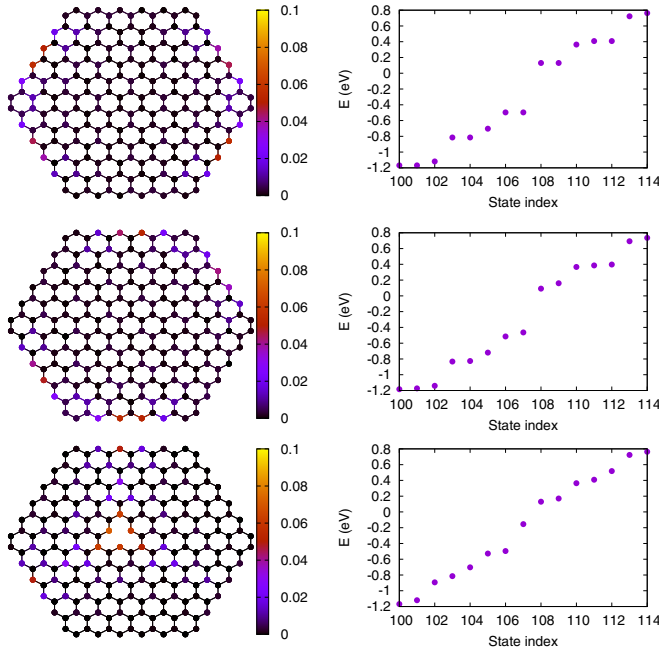
---
[*]mkrtchian@ysu.am

FIG. 1. The top row represents intrinsic GQD_{216}, the middle row depicts GQD_{216} with disorder, and the bottom row illustrates GQD_{216} with a monovacancy. Within each row, the following visualizations are presented from left to right: electron probability density corresponding to the highest energy level in the valence band and eigenenergies near the Fermi level.

The investigation of the intersection between strong-field attosecond science and condensed matter has revealed that HHG spectroscopy is a versatile tool for the all-optical exploration of the structural, topological, and dynamical properties of novel nanostructures [63,64]. This technique proves particularly effective in probing topological phase transitions [65–68] and reconstructing Berry curvatures of bands through the observation of anomalous harmonics [69,70]. Recent studies have demonstrated that an imperfect lattice can lead to enhancement of HHG compared to a perfect lattice, particularly when considering doping-type impurities or disorder [46,71–74]. Specific types of spatial defects, such as vacancies and adatoms in graphene can turn monolayer graphene into a topological material [75]. A single vacancy induces a localized stable charge of order unity, inducing zero energy states at the Dirac point and connecting these modes to vacuum fractional charge and a parity anomaly [76]. These findings prompt the question of how the disorder or vacancies specifically affect the HHG spectra in GQDs. It is worth noting that GQDs with sharp boundaries exhibit time-reversal symmetry breaking even in the absence of a magnetic field [6], suggesting the possibility of Hall-type anomalous responses in both linear and nonlinear regimes for imperfect GQDs. In this study we present a microscopic theory that explores the linear and nonlinear interaction of GQDs with strong coherent electromagnetic radiation in the presence of on-site disorder or vacancy. Specifically, we investigate hexagonal GQD with a moderate size, as illustrated in Fig. 1. By employing up to 10th-nearest-neighbor hopping integrals within a dynamical Hartree-Fock (HF)

approximation, we reveal the polarization-resolved structure of the HHG spectrum.

The paper is organized as follows. In Sec. II the model with the basic equations are formulated. In Sec. III the linear optical response is considered. In Sec. IV we present the results regarding nonlinear optical response. Finally, conclusions are given in Sec. V.

II. THE MODEL

The basic GQD_{216}, illustrated in Fig. 1, has symmetry described by the non-Abelian point group C_{6v}. We also consider GQD_{216} with on-site disorder and GQD_{216} with a monovacancy. GQD is assumed to interact with a laser pulse that excites electron coherent dynamics. We assume a neutral GQD that will be described in the scope of the tight-binding (TB) theory. Hence the total Hamiltonian reads

$$\widehat{H} = \widehat{H}_{TB} + \widehat{H}_{C} + \widehat{H}_{int}, \tag{1}$$

where

$$\widehat{H}_{TB} = \sum_{i\sigma} \varepsilon_i c_{i\sigma}^\dagger c_{i\sigma} - \sum_{i,j\sigma} t_{ij} c_{i\sigma}^\dagger c_{j\sigma} \tag{2}$$

is the free GQD TB Hamiltonian. Here $c_{i\sigma}^\dagger$ ($c_{i\sigma}$) creates (annihilates) an electron with the spin polarization $\sigma = \{\uparrow, \downarrow\}$ at site i ($\overline{\sigma}$ is the opposite to σ spin polarization). In Eq. (2) ε_i is the energy level at site i, and t_{ij} is the hopping integral between sites i and j.

The second term in the total Hamiltonian (1) describes the electron-electron interaction (EEI):

$$\widehat{H}_C = \frac{U}{2} \sum_{i\sigma} c_{i\sigma}^\dagger c_{i\sigma} c_{i\overline{\sigma}}^\dagger c_{i\overline{\sigma}} + \frac{1}{2} \sum_{i,j\sigma\sigma'} V_{ij} c_{i\sigma}^\dagger c_{i\sigma} c_{j\sigma'}^\dagger c_{j\sigma'}, \tag{3}$$

with the parameters U and V_{ij} representing the on-site and long-range Coulomb interactions, respectively. The last term in the total Hamiltonian (1) is the light-matter interaction part that is described in the length gauge:

$$\widehat{H}_{int} = e \sum_{i\sigma} \mathbf{r}_i \cdot \mathbf{E}(t) c_{i\sigma}^\dagger c_{i\sigma}, \tag{4}$$

with the elementary charge e, position vector $\mathbf{r}_i$, and the electric field strength $\mathbf{E}(t)$.

In this work, EEI is treated in the HF mean-field approximation employing the correlation expansion

$$\langle c_1^\dagger c_2^\dagger c_3 c_4 \rangle = \langle c_1^\dagger c_4 \rangle \langle c_2^\dagger c_3 \rangle - \langle c_1^\dagger c_3 \rangle \langle c_2^\dagger c_4 \rangle.$$

This factorization technique allows us to obtain a closed set of equations for the single-particle density matrix $\rho_{ji}^{(\sigma)} = \langle c_{i\sigma}^\dagger c_{j\sigma} \rangle$. We will assume that in the static limit the EEI Hamiltonian vanishes $\widehat{H}_C^{HF} \simeq 0$. That is, EEI in the HF limit is included nonexplicitly in the empirical TB parameters $\widetilde{\varepsilon}_i$, $\widetilde{t}_{ij}$, which is chosen to be close to experimental values. For this propose in this paper we use up to 10th-nearest-neighbor hopping $\widetilde{t}_{ij}$ with values taken from density functional theory by Wannierization [77] (see Table I). Hence, the Hamiltonian

TABLE I. The first row represents nth-nearest-neighbor order. The second row is the set of tight-binding parameters, where $t_{ii} = \widetilde{\epsilon}_0$. The third row is the Coulomb interaction matrix elements. The first three elements, where $U = V_{ii}$, are obtained from numerical calculations by using Slater π_z orbitals [22,78]. The longer range Coulomb interaction is taken to be $\epsilon_d V_{ij} = 14.4/d_{ij}$ eV, where d_{ij} is the distance in angstroms between the distant neighbors. Here ϵ_d is an effective dielectric constant which accounts for the substrate-induced screening in the 2D nanostructure.

Nearest neighbor	0	1	2	3	4	5	6	7	8	9	10
t_{ij} [eV]	0.297	2.912	−0.223	0.289	−0.025	−0.055	0.022	0.013	0.022	−0.007	−0.004
$\epsilon_d V_{ij}$ [eV]	16.5	8.6	5.3	$14.4/d_{i3}$	$14.4/d_{i4}$	$14.4/d_{i5}$	$14.4/d_{i6}$	$14.4/d_{i7}$	$14.4/d_{i8}$	$14.4/d_{i9}$	$14.4/d_{i10}$

$\widehat{H}_{TB} + \widehat{H}_C$ is approximated by

$$\widehat{H}_0^{HF} = \sum_{i\sigma} \widetilde{\varepsilon}_i c_{i\sigma}^\dagger c_{i\sigma} - \sum_{i,j\sigma} \widetilde{t}_{ij} c_{i\sigma}^\dagger c_{j\sigma} + U \sum_i (\overline{n}_{i\uparrow} - \overline{n}_{0i\uparrow}) n_{i\downarrow}$$

$$+ U \sum_{i\sigma} (\overline{n}_{i\downarrow} - \overline{n}_{0i\downarrow}) n_{i\uparrow} + \sum_{\langle i,j\rangle} V_{ij}(\overline{n}_j - \overline{n}_{0j}) n_i$$

$$- \sum_{i,j\sigma} V_{ij} c_{i\sigma}^\dagger c_{j\sigma} (\langle c_{i\sigma}^\dagger c_{j\sigma}\rangle - \langle c_{i\sigma}^\dagger c_{j\sigma}\rangle_0), \qquad (5)$$

where $\overline{n}_{i\sigma} = \langle c_{i\sigma}^\dagger c_{i\sigma}\rangle = \rho_{ii}^{(\sigma)}$. In this representation the initial density matrix $\rho_{ji}^{(\sigma)}(0) = \langle c_{i\sigma}^\dagger c_{j\sigma}\rangle_0$ is calculated with respect to the renormalized tight-binding Hamiltonian $\widehat{H}_0^t = -\sum_{i,j\sigma} \widetilde{t}_{ij} c_{i\sigma}^\dagger c_{j\sigma}$. From the Heisenberg equation we obtain evolutionary equations for the single-particle density matrix $\rho_{ij}^{(\sigma)} = \langle c_{j\sigma}^\dagger c_{i\sigma}\rangle$:

$$i\hbar \frac{\partial \rho_{ij}^{(\sigma)}}{\partial t} = \sum_k \left(\tau_{kj\sigma} \rho_{ik}^{(\sigma)} - \tau_{ik\sigma} \rho_{kj}^{(\sigma)}\right) + (V_{i\sigma} - V_{j\sigma})\rho_{ij}^{(\sigma)}$$

$$+ e\mathbf{E}(t)(\mathbf{r}_i - \mathbf{r}_j)\rho_{ij}^{(\sigma)} - i\hbar\gamma\left(\rho_{ij}^{(\sigma)} - \rho_{0ij}^{(\sigma)}\right), \quad (6)$$

where

$$V_{i\sigma} = \sum_{j\alpha} V_{ij}\left(\rho_{jj}^{(\alpha)} - \rho_{0jj}^{(\alpha)}\right) + U\left(\rho_{ii}^{(\overline{\sigma})} - \rho_{0ii}^{(\overline{\sigma})}\right), \qquad (7)$$

and

$$\tau_{ij\sigma} = -\widetilde{\varepsilon}_i \delta_{ij} + \widetilde{t}_{ij} + V_{ij}\left(\rho_{ji}^{(\sigma)} - \rho_{0ji}^{(\sigma)}\right). \qquad (8)$$

Electron-electron, electron-phonon scattering processes have been introduced in Eq. (6) phenomenologically via the damping term, assuming that the system relaxes at a rate γ to the equilibrium $\rho_{0ij}^{(\sigma)}$ distribution.

In the present paper, as a first approximation, monovacancy is simulated by setting the hopping parameters to the empty site to zero, and the on-site energy at the empty site equals a large value outside the energy range of the density of states [79]. There is also a scenario when the structure undergoes a bond reconstruction in the vicinity of the vacancy [80]. In either case, a local distortion of the lattice takes place, resulting in states that are strongly localized around defects [81,82]. In the tight-binding Hamiltonian (5), the diagonal disorder is described by the Anderson model introducing randomly distributed site energies ϵ_{ri}: $\widetilde{\epsilon}_i = \widetilde{\epsilon}_{0i} + \epsilon_{ri}$. We assume for the random variable ϵ_{ri} to have probability distributions $P(\epsilon_{ri}, V_{on})$, where

$$P(\epsilon_{ri}, V_{on}) = \begin{cases} \frac{1}{2V_{on}}, & -V_{on} \leqslant \epsilon_{ri} \leqslant V_{on} \\ 0, & \text{otherwise} \end{cases}. \qquad (9)$$

Here the quantity V_{on} is the distribution width describing the strength of the disorder. The disorder strength for all calculations is taken to be $V_{on} = 0.3$ eV.

III. LINEAR OPTICAL RESPONSE

The linear optical response of the considered system is completely described by the initial equilibrium $\rho_{0ij}^{(\sigma)}$ distribution function. For this propose we need the eigenfunctions ($\psi_{\sigma\mu}(i)$) and eigenenergies ($\varepsilon_{\sigma\mu}$) of the TB Hamiltonian. We numerically diagonalize the TB Hamiltonian with the parameters from Table I and construct the initial density matrix $\rho_{0ij}^{(\sigma)}$ via the filling of electron states in the valence band according to the zero-temperature Fermi-Dirac distribution $\rho_{0ij}^{(\sigma)} = \sum_{\mu=N/2}^{N-1} \psi_{\sigma\mu}^*(j)\psi_{\sigma\mu}(i)$. In Fig. 1 the electron probability density $|\psi_{\sigma\mu}(i)|^2$ on the 2D color-mapped nanostructure corresponding to the highest energy level in the valence band and eigenenergies near the Fermi level are shown. In both cases we see the emergence of states near the Fermi level. As is also seen from this figure, the presence of on-site disorder or a monovacancy breaks the inversion symmetry. As expected, in the case of a vacancy we have a state that is strongly localized around the defect. To provide a quantitative characterization of localization in the μth eigenstates, we also calculate the inverse participation number

$$P_\mu = \left(\sum_{i=0}^{N-1} |\psi_\mu(i)|^4\right)^{-1}, \qquad (10)$$

which provides a measure of the fraction of sites over which the wave packet is spread [83]. The energy spectra for the systems under consideration are illustrated in Fig. 2(a). The color bar indicates normalized inverse participation numbers P_μ/N for states. Figure 2(b) shows inverse participation numbers P_μ/N for states near the Fermi level. The energy spectra depicted in Fig. 2(a) demonstrate that they are nearly identical for the intrinsic, vacancy, and disorder-defected cases. Highly excited states are delocalized $P_\mu/N \sim 0.5$, which means that those states are more resistant to defects. However, notable changes in the spectra and symmetries of states occur in proximity to the Fermi level, Fig. 2(b). From this figure it becomes evident that these states are localized, which as we will see, strongly alters the optical response of the considered nanostructures.

To study the linear response we first need to calculate the susceptibility tensor χ_{ij}, which is more transparent to give in the energetic representation. For this propose we perform a
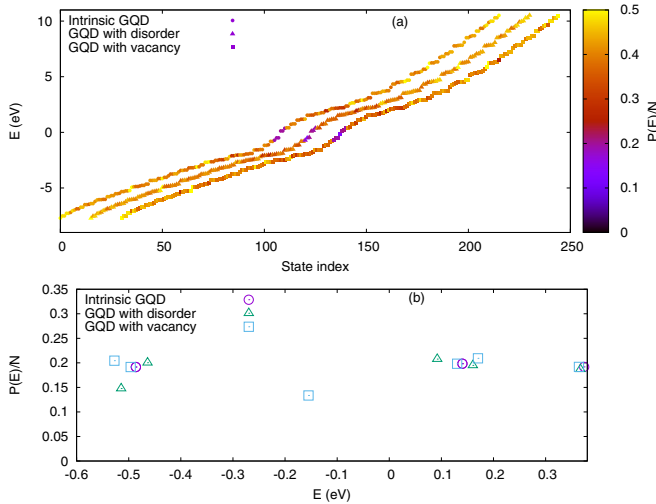
FIG. 2. The energy spectra for the systems under consideration are depicted in (a). To enhance clarity, the state indexes for the disorder and monovacancy cases are shifted. The color bar represents the normalized inverse participation numbers P_μ/N for states. For a closer examination, a zoomed-in view is presented in (b), illustrating the normalized inverse participation numbers for states near the Fermi level.

basis transformation using the following formula:

$$\rho_{ij}^{(\sigma)} = \sum_{\mu'} \sum_{\mu} \psi_{\sigma\mu'}^*(j) \varrho_{\sigma\mu\mu'} \psi_{\sigma\mu}(i), \tag{11}$$

where $\varrho_{\sigma\mu\mu'}$ is the density matrix in the energetic representation. Taking into account the completeness of basis functions, from Eq. (6) we get the following equation:

$$i\hbar \frac{\partial \varrho_{\sigma mn}}{\partial t} = (\varepsilon_{\sigma m} - \varepsilon_{\sigma n}) \varrho_{\sigma mn}$$

$$+ \mathbf{E}(t) \sum_{\mu} (\varrho_{\sigma\mu n} \mathbf{d}_{\sigma m\mu} - \varrho_{\sigma m\mu} \mathbf{d}_{\sigma\mu n})$$

$$- i\hbar\gamma \left(\varrho_{\sigma mn} - \varrho_{\sigma mn}^{(0)} \right), \tag{12}$$

where $\mathbf{d}_{\sigma\mu'\mu} = e \sum_i \psi_{\sigma\mu'}^*(i) \mathbf{r}_i \psi_{\sigma\mu}(i)$ is the transition dipole moment. We will solve Eq. (12) in the scope of perturbation theory by expanding the density matrix in orders of the incident electromagnetic field:

$$\varrho_{\sigma mn} = \varrho_{\sigma mn}^{(0)} + \varrho_{\sigma mn}^{(1)}. \tag{13}$$

Assuming $E_j(t) = \sum_\omega E_j(\omega) e^{-i\omega t}$, it is straightforward to obtain

$$\varrho_{\sigma mn}^{(1)} = \sum_{j\omega} \frac{E_j(\omega) e^{-i\omega t} d_{\sigma mn}^j \left(\varrho_{\sigma nn}^{(0)} - \varrho_{\sigma mm}^{(0)} \right)}{\varepsilon_{\sigma m} - \varepsilon_{\sigma n} - \hbar\omega - i\hbar\gamma}.$$

The polarization vector $P_i(t) = \sum_{\sigma mn} \varrho_{\sigma mn}^{(1)}(t) d_{\sigma nm}^i$ now can be expressed as

$$P_i(t) = \sum_{\sigma mn} \sum_{j\omega} \frac{E_j(\omega) e^{-i\omega t} d_{\sigma mn}^j \left(\varrho_{\sigma nn}^{(0)} - \varrho_{\sigma mm}^{(0)} \right)}{\varepsilon_{\sigma m} - \varepsilon_{\sigma n} - \hbar\omega - i\hbar\gamma}. \tag{14}$$

Taking into account the definition $P_i = \epsilon_0 \sum_j \chi_{ij} E_j$, where ϵ_0 is the electric permittivity of free space, from Eq. (14)

we get

$$\chi_{ij}(\omega) = \frac{1}{\epsilon_0} \sum_{\sigma mn} \varrho_{\sigma mm}^{(0)} \left[\frac{d_{\sigma nm}^j d_{\sigma mn}^i}{\varepsilon_{\sigma n} - \varepsilon_{\sigma m} - \hbar\omega - i\hbar\gamma} \right.$$

$$\left. + \frac{d_{\sigma mn}^j d_{\sigma nm}^i}{\varepsilon_{\sigma n} - \varepsilon_{\sigma m} + \hbar\omega + i\hbar\gamma} \right]. \tag{15}$$

With the help of susceptibility tensors in SI units, we also calculate the conductivity tensors in cgs units by the formula

$$\sigma_{ij}(\omega) = -i\epsilon_0 \omega \chi_{ij}(\omega). \tag{16}$$

The tensor $\sigma_{ij}(\omega)$ can be dissected into symmetric and antisymmetric components. For 2D systems, there exists a single independent component that characterizes the antisymmetric conductivity: $\sigma_{xy}(\omega) = -\sigma_{yx}(\omega)$. This component is commonly known as the dissipationless or Hall conductivity, denoted as $\sigma_H(\omega)$. Under spatial symmetry transformations, the Hall component transforms as a pseudoscalar [84], given by $\sigma_H(\omega) = \det(O) \sigma_H(\omega)$. Consequently, the Hall conductivity becomes zero in systems with mirror symmetry, where $\det(O) = -1$. Furthermore, it also vanishes in time-reversal invariant systems. To observe a nonzero Hall component in the considered GQD, it is imperative to break both time-reversal and inversion symmetries. The time-reversal symmetry can be disrupted, for example, through the application of a magnetic field. Remarkably, in the context of GQDs characterized by sharp boundaries, the time-reversal symmetry is inherently broken even in the absence of an external magnetic field [6]. This intriguing property hints at the potential for Hall-type anomalous responses in such imperfect GQDs. For the purposes of our analysis, we neglect spin effects and assume a zero-temperature Fermi-Dirac distribution for the initial density matrix $\varrho_{\sigma mm}^{(0)}$. Under these conditions, the expressions for the conduction tensor can be derived from Eqs. (15) and (16) as follows:

$$\sigma_{ij}(\omega) = -2i\omega \sum_{m \in v} \sum_{n \in c} d_{nm}^j d_{mn}^i \left[\frac{1}{\varepsilon_n - \varepsilon_m - \hbar\omega - i\hbar\gamma} \right.$$

$$\left. + \frac{1}{\varepsilon_n - \varepsilon_m + \hbar\omega + i\hbar\gamma} \right]. \tag{17}$$

As evident from Eq. (17), the conduction tensor is primarily defined by the joint density of states (JDS),

$$JDS = \sum_{m \in v} \sum_{n \in c} \delta(\varepsilon_n - \varepsilon_m - \hbar\omega),$$

and the values of the product $d_{nm}^j d_{mn}^i$ of the interband transition dipole matrix elements. In Fig. 3 we illustrate the JDS and the absolute values of the product of the x and y components of the interband transition dipole matrix elements. As is seen from this figure, the influence of on-site disorder and a monovacancy on GQD$_{216}$ is nearly identical. While the JDS is somewhat suppressed, both factors lift the degeneracy of states and break the inversion symmetry, thereby opening up new channels for interband transitions. The product $d_{cv}^x d_{cv}^y$ has several peaks near the particular interband transitions, which means that near these peaks one can expect a strong Hall-type
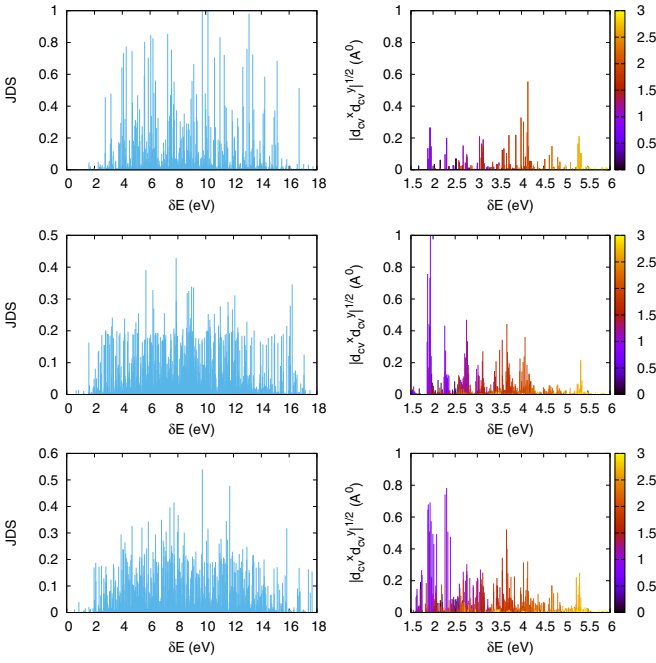
FIG. 3. The top panel represents intrinsic GQD$_{216}$, the middle panel depicts GQD$_{216}$ with disorder, and the bottom panel illustrates GQD$_{216}$ with a monovacancy. The left column is the joint density of states, and the right column is the absolute values of the product of the x and y components of interband transition dipole matrix elements. The color boxes indicate the energy ranges (in eV) of the conduction bands.
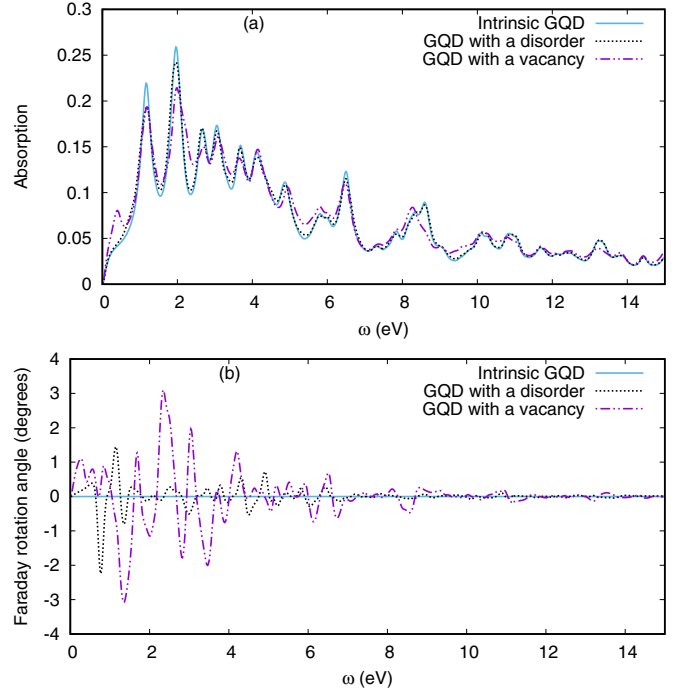

FIG. 4. Linear optical response of GQD via absorption coefficient (a) and Faraday-rotation angle (b). The relaxation rate is set to $\hbar\gamma = 0.1$ eV. The dielectric constant of the substrate is taken to be $\epsilon_d = 6$.

anomalous response. To assess the consequences of the linear response using $\sigma_{ij}(\omega)$, we will compute the linear absorption coefficient and the Faraday-rotation angle. For both quantities we will use formulas derived for graphene at normal incidence of a laser beam. The linear absorption coefficient is defined through the diagonal component of conductivity [85]:

$$\alpha_{\mathrm{abs}} = \frac{4\pi}{c} \frac{\mathrm{Re}\,\sigma_{xx}(\omega)}{\left| \frac{\sqrt{\epsilon}+1}{2} + 2\pi\sigma_{xx}(\omega)/c \right|^2}, \qquad (18)$$

while the Faraday-rotation angle Θ_F is related to the optical Hall conductivity [86] through the formula

$$\Theta_F = \frac{1}{2}\arg\left[\frac{1 + \sqrt{\epsilon} + \frac{4\pi}{c}[\sigma_{xx}(\omega) + i\sigma_{xy}(\omega)]}{1 + \sqrt{\epsilon} + \frac{4\pi}{c}[\sigma_{xx}(\omega) - i\sigma_{xy}(\omega)]} \right]. \qquad (19)$$

Here c represents the velocity of light, and ϵ denotes the dielectric constant of the substrate. Strictly speaking, the absorption coefficient and Faraday-rotation angle are meaningful for a nanostructure layer with dimensions much larger than the incident light wavelength. In other words, we should have many copies of the GQDs uniformly distributed on a 2D surface. We investigate these quantities to emphasize the consequences of disorder or vacancies on the optical response of GQDs. In Fig. 4 we present the linear optical response of GQD$_{216}$ in terms of the absorption coefficient and Faraday-rotation angle. Notably, the absorption coefficient is minimally affected by disorder or vacancies. This is due to the fact that the absorption coefficient primarily depends on the energy spectra, which, with the exception of

the spectra near the Fermi level, are practically the same in the cases under consideration Fig. 2(a), and any distinctive variations in the spectra are diminished for the selected relaxation rate. In comparison to graphene, where $\alpha_{\mathrm{abs}} \approx \pi/137$, we observe a significantly higher absorption ($\alpha_{\mathrm{abs}} \sim 0.1$). In terms of Hall-type anomalous response, we observe a substantial Faraday-rotation angle for monovacancy and a less pronounced effect for disorder. As expected, intrinsic GQD displays a Faraday-rotation angle of zero. It is worth noting that the maximal angle induced by a monovacancy, $\Theta_F \sim 3^\circ$, is comparable to the Faraday-rotation angle of graphene in the strong magnetic field with strengths ~3 T [87]. In this paper when referring to Hall-type anomalous response, we are drawing an analogy to the quantum anomalous Hall effect [88], which manifests in the absence of external magnetic fields due to the spontaneous breaking of time-reversal symmetry. Namely, in our system we have spontaneous breaking of time-reversal symmetry.

IV. NONLINEAR OPTICAL RESPONSE

After considering the linear response, we begin by examining the nonlinear optical response of GQD$_{216}$ in the strong infrared laser field described by the electric field strength $\mathbf{E}(t) = f(t)E_0\hat{\mathbf{e}}\cos\omega t$, with the frequency ω, polarization $\hat{\mathbf{e}}$ unit vector, and amplitude E_0. The wave envelope is described by the Gaussian function $f(t) = \exp[-2\ln 2(t - t_m)^2/\mathcal{T}^2]$, where $\mathcal{T}$ characterizes the pulse duration full width at half maximum, and t_m defines the position of the pulse maximum. Note that for the Gaussian envelope the number of oscillations

N_s of the field is approximated as $\mathcal{T}/T \simeq 0.307 N_s$, where $T = 2\pi/\omega$ is the wave period (4.135 fs for 1 eV).

To compute the harmonic signal, we use the Fourier transform

$$\mathbf{a}(\Omega) = \int_{-\infty}^{\infty} \mathbf{a}(t)e^{i\Omega t}W(t)dt, \qquad (20)$$

where

$$\mathbf{a}(t) = e\sum_{i\sigma} \mathbf{r}_i \frac{d^2}{dt^2}\rho_{ii}^{(\sigma)}(t) \qquad (21)$$

is the dipole acceleration and $W(t)$ is a window function that suppresses small fluctuations and reduces the overall background noise of the harmonic signal [89]. We choose the pulse envelope $f(t)$ as the window function. For all further calculations we assume a polarization unit vector $\hat{\mathbf{e}} = \{1, 0\}$, and the pulse duration $\mathcal{T}$ is set to $\mathcal{T}/T \simeq 3$, corresponding to approximately ten oscillations ($N_s \simeq 10$). To ensure a smooth turn-on of the interaction, we position the pulse center at $t_m = 10T$. For convenience, we normalize the dipole acceleration by the factor $a_0 = e\overline{\omega}^2\overline{d}$, where $\overline{\omega} = 1$ eV$/\hbar$ and $\overline{d} = 1$ Å. The power radiated at a given frequency is proportional to $S(\Omega) = |\mathbf{a}(\Omega)|^2/a_0^2$. We perform the time integration of Eq. (6) using the eighth-order Runge-Kutta algorithm. For the Coulomb interaction matrix elements we take values from Table I and the dielectric constant of the substrate is taken to be $\epsilon_d = 6$.

To begin with, we examine the effect of the monovacancy and disorder on the HHG spectra. The HHG spectra are compared for three different scenarios in Fig. 5: when we have the intrinsic GQD$_{216}$, when the GQD$_{216}$ has a monovacancy, and when it is subject to on-site disorder. The inclusion of a monovacancy or disorder leads to two noteworthy characteristics in the HHG spectra: (a) the most prominent feature is the emergence of even harmonics comparable to odd harmonics, and (b) substantial increase in the HHG signal in the vicinity of the cutoff regime. The first phenomenon is attributed to the special inversion symmetry breaking in the presence of disorder and vacancy. The second phenomenon is connected with the fact that the disorder and vacancy lift the degeneracy of states, opening up new channels for interband transitions.

To reveal the inherent effects of broken time-reversal symmetry on the nonlinear response, we conducted an investigation into polarization-resolved HHG spectra. In Fig. 6 we present the polarization-resolved HHG spectra for GQD$_{216}$ with disorder and for GQD$_{216}$ featuring a monovacancy. This figure highlights a significant finding, especially in the case of a monovacancy where even-order harmonics shown in Fig. 5 manifest as Hall-type anomalous harmonics polarized perpendicular to the direction of applied laser electric field. Importantly, due to the simultaneous breaking of time and inversion symmetry in Fig. 6, there is a concurrent observation of even harmonics aligned with the polarization direction of the pump laser, although with suppression, and odd Hall-type anomalous harmonics in the perpendicular direction. In this context, to avoid confusion it is necessary to clarify that in extended systems, anomalous harmonics specifically refer to harmonics originating from a nonzero Berry curvature of bands [70]. In cases where time-reversal symmetry is
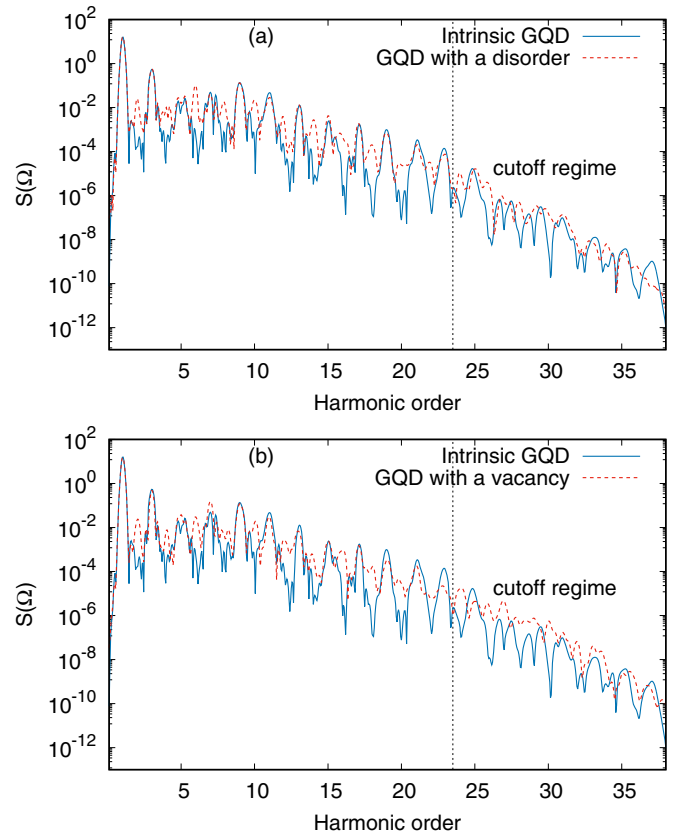

FIG. 5. The total HHG spectra in logarithmic scale (in arbitrary units) for GQD$_{216}$ with a disorder (a) and for GQD$_{216}$ with monovacancy (b) along with the HHG spectra of intrinsic GQD. The dashed vertical line demarcates the cut-off segment of harmonics from the plateau harmonics. The wave amplitude is taken to be $E_0 = 0.3$ V/Å. The relaxation rate is set to $\hbar\gamma = 0.1$ eV. The excitation is performed assuming a laser with a wavelength of 2.48 μm, an excitation frequency of $\omega = 0.5$ eV$/\hbar$.

maintained, resulting in a Chern number of zero for the entire Brillouin zone, only even anomalous harmonics are allowed. Conversely, when inversion symmetry is preserved but time-reversal symmetry is broken, only odd anomalous harmonics are permitted [90]. Given that our investigation centers on a GQD, relying on Berry curvature physics, which is more applicable to extended systems with clearly defined Bloch bands, is not appropriate. Consequently, we term the observed perpendicular harmonics as "Hall-type anomalous" to underscore their absence in the intrinsic case and their emergence as a consequence of the simultaneous breaking of time and inversion symmetry.

Of specific interest is the plateau region within the harmonics spectra. In Fig. 7 we present the plateau portion of the anomalous HHG spectrum of GQD$_{216}$ with a monovacancy for various wave field amplitudes. In this representation, none of the harmonics conform to the perturbation scaling $S^{1/2}(n\omega) \sim E_0^n$. This observation underscores the strictly multiphoton and nonlinear nature of the HHG process.

Now, let us consider the effect of the pump wave frequency on the Hall-type anomalous HHG process. This analysis is presented in Fig. 8 where we demonstrate the
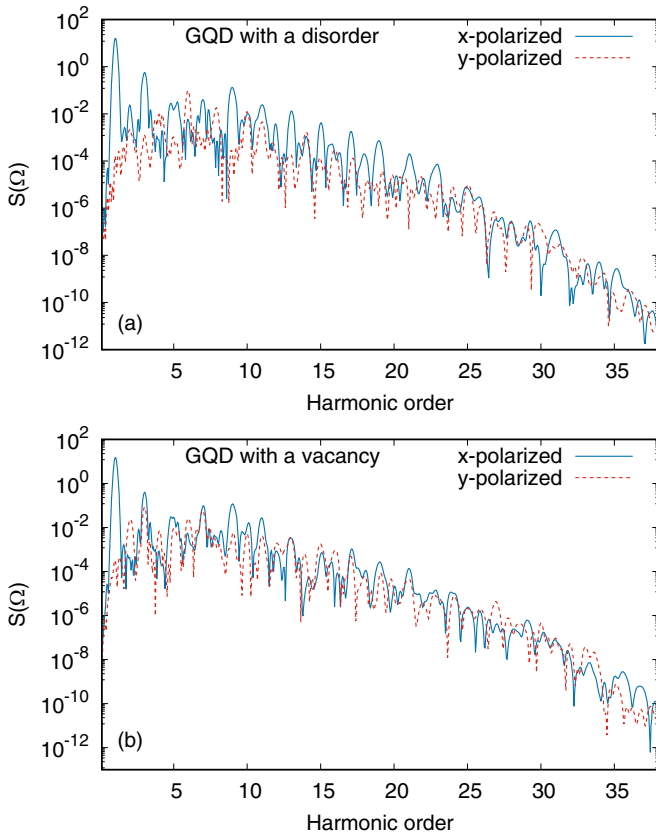
FIG. 6. The polarization-resolved HHG spectra in logarithmic scale for GQD_{216} with a disorder (a) and for GQD_{216} with a monovacancy (b). The laser parameters correspond to Fig. 5.

FIG. 8. The polarization-resolved HHG spectra in logarithmic scale for GQD_{216} with a monovacancy for $\omega = 1.0$ eV/$\hbar$ (a) and $\omega = 1.5$ eV/$\hbar$ (b). The wave amplitude is taken to be $E_0 = 0.3$ V/Å. The relaxation rate is set to $\hbar\gamma = 0.1$ eV.

polarization-resolved HHG spectra for higher-frequency laser fields. Notably, we observe that the rate of anomalous harmonics is suppressed for higher-frequency pump waves. This phenomenon can be attributed to the fact that with higher-frequency pump waves, excitation and recombination channels predominantly involve highly excited states that are delocalized [see Fig. 2(a)] and in average retain inversion symmetry.

To gain deeper insights into the underlying causes of the anomalous harmonics, we employ a wavelet transform [91] of
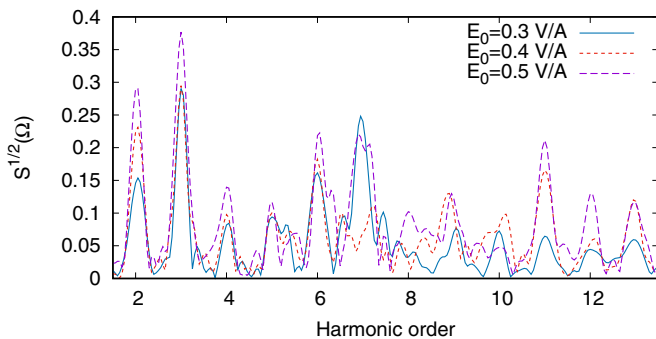

FIG. 7. The plateau part of the anomalous HHG spectrum of GQD_{216} with a monovacancy is presented in the linear scale for various wave field amplitudes. The excitation frequency is taken to be $\omega = 0.5$ eV/$\hbar$.
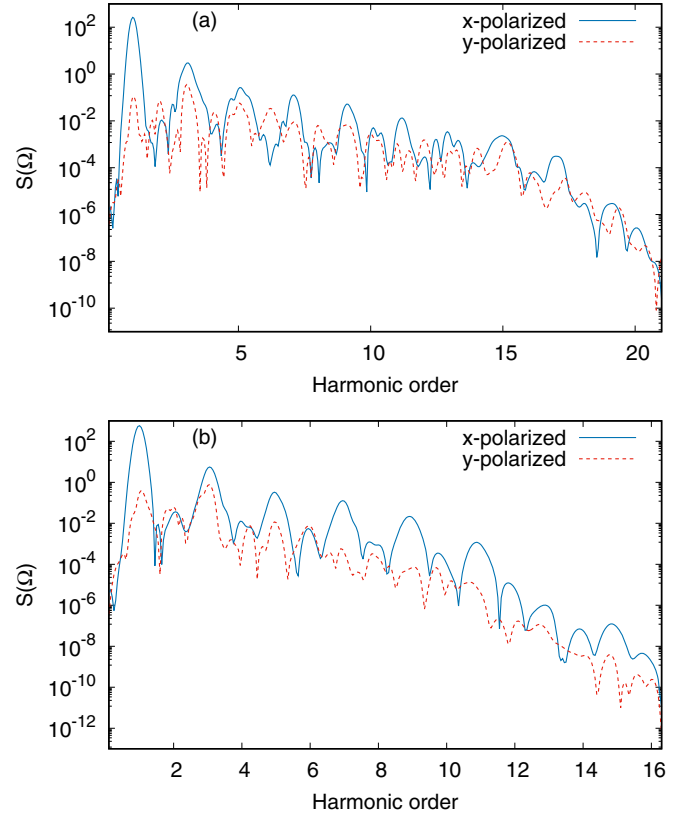
the dipole acceleration to perform a time-frequency analysis. We utilize the Morlet transform ($\sigma = 10$) of the dipole acceleration, given by

$$\mathbf{a}(t, \Omega) = \sqrt{\frac{\Omega}{\sigma}} \int_0^\tau dt' \mathbf{a}(t) e^{i\Omega(t'-t)} e^{-\frac{\Omega^2}{2\sigma^2}(t'-t)^2}. \quad (22)$$

Figure 9 illustrates the time-frequency analysis for normal harmonics (a) and anomalous harmonics (b). It also displays the time evolution of the population of the highest energy level in the valence band. Time profiles for the low harmonics exhibit a sufficiently smooth variation over time and are not plotted. Two distinct patterns are observed in this figure. Specifically, for normal harmonics, bursts are produced with a period of $0.5T$, consistent with HHG in atomic systems and solid-state harmonics. Meanwhile, for anomalous harmonics, bursts are predominantly produced around integer multiples of the optical period. This difference in the time-frequency spectra can be explained by considering the populations of the occupied states near the Fermi level. At the turn-on of the interaction, mainly these states are depopulated into the excited states, and HHG occurs when the transition from the excited states back to the depopulated states takes place. Hence, emission times of harmonics should coincide with the local maximums in the population time profile of the depopulated states. These local maximums coincide with the zeros of the electric field, while local minimums coincide with the peaks of the electric field. As seen from Fig. 9(a) for normal
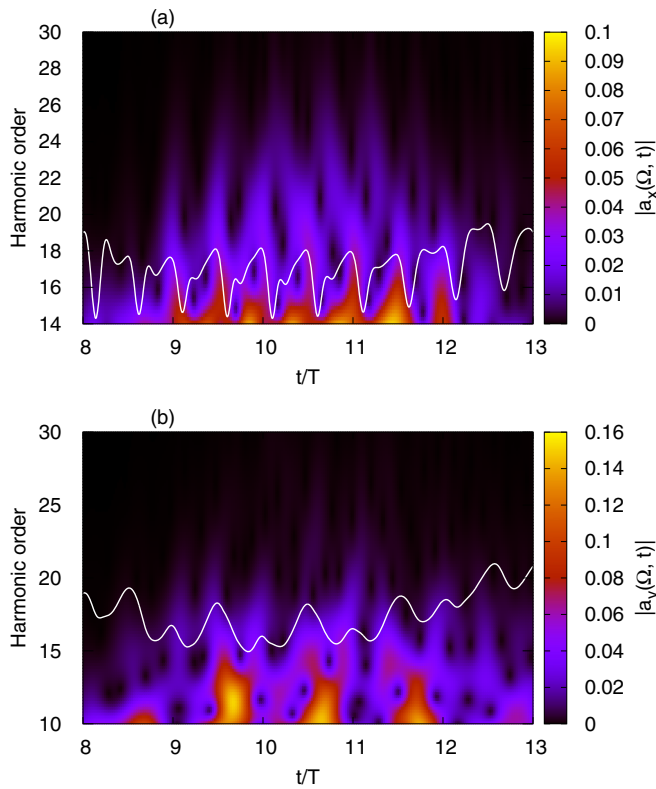
FIG. 9. The spectrogram of the HHG process via the wavelet transform of the dipole acceleration $a_x(t, \Omega)$ for intrinsic GQD_{216} (a) and $a_y(t, \Omega)$ for GQD_{216} with a monovacancy (b). The time interval where the wave's amplitude is considerable is shown. The laser parameters align with those in Fig. 5. The color bar is presented in the linear scale in arbitrary units. White solid lines overlaid on the density plot depict the time evolution of the population of the highest energy level in the valence band, rescaled for visual clarity.

harmonics, this tendency is mainly preserved. For anomalous harmonics, due to the inversion symmetry breaking, the states near the Fermi level acquire a huge permanent dipole moment d_{mean}, giving rise to linear dynamic Stark shifts of energy levels $\sim d_{mean}E(t)$ that maximize or minimize the transition to excited states depending on the sign which changes after half of the period. Hence, in Fig. 9(b) we observe that one of the local peaks in the population time profile during the full period dominates. Note that for intrinsic GQD_{216}, $d_{mean} = 0$ for all states, while for the state under consideration, $d_{mean}/e \simeq 2\mathring{A}$, and the Stark shift amplitude is comparable to the pump wave photon energy. A similar behavior in the time evolution of population dynamics is observed for a maximally localized state near the Fermi level in GQD_{216} with disorder.

V. CONCLUSION

We have studied the character and specifics of linear and nonlinear optical response of hexagonal GQDs in the presence of on-site disorder or vacancies. Our primary focus was on medium-sized GQDs composed of 216 carbon atoms, which in their defectless state possess inversion symmetry. To model a disorder, we employed the Anderson model, while for monovacancies we utilized a simplified model by setting the hopping parameters to the empty site to zero and assigning a large value to the on-site energy at the empty site. In our TB model, we considered up to the 10th-nearest-neighbor hopping elements. Electron-electron interactions were treated within the HF approximation, incorporating the long-range Coulomb interactions. Through the solution of the evolutionary equations for the single-particle density matrix, we revealed anomalous optical responses in defective GQDs across both linear and nonlinear interaction regimes. In linear response, in the absence of an external magnetic field we observed a significant Hall conductivity, resulting in a substantial Faraday-rotation angle. This phenomenon is attributed to the intrinsic time-reversal symmetry breaking in graphene quantum dots, coupled with the simultaneous breaking of spatial inversion symmetry in the presence of disorder or monovacancies. The combined disruption of time-reversal and inversion symmetries leads to the emergence of intense Hall-type anomalous HHG. Notably, these anomalous high harmonics are more pronounced in low-frequency laser fields. In such scenarios, excitation and recombination channels predominantly involve states near the Fermi level that are more susceptible to inversion symmetry breaking.

Our study highlights the sensitivity of Hall-type anomalous high harmonics to even minor levels of disorder or the presence of a monovacancy, providing an appropriate means for optical characterization of defects in 2D nanostructures. The investigation specifically becomes significant when extending the analysis to multiple vacancies where diverse phenomena are anticipated. In the context of an infinite graphene sheet composed of two sublattices, A and B, and in the presence of $N_A + N_B$ vacancies (N_A, N_B are the number of vacancies corresponding to sublattices A and B, respectively), the tight-binding Hamiltonian reveals $|N_A - N_B|$ zero-energy eigenvalues with vanishing wave functions on the minority sublattice [55,92]. This effect persists regardless of the relative position of the vacancies and has a long-term impact of a topological nature, connecting zero modes to vacuum fractional charge and a parity anomaly [93]. Parity symmetry is restored when there is an equal number of A and B vacancies [76]. Therefore, to magnify the observed effects, especially the strengths of anomalous harmonics, it becomes actual to consider multiple vacancies from the same sublattice. In our study, we concentrated on a relatively small GQD that permits the consideration of these phenomena via HHG spectroscopy. The obtained results demonstrate the efficiency of HHG spectroscopy as a powerful tool in this topic.

[1] P. R. Wallace, The band theory of graphite, Phys. Rev. **71**, 622 (1947).

[2] G. W. Semenoff, Condensed-matter simulation of a three-dimensional anomaly, Phys. Rev. Lett. **53**, 2449 (1984).

[3] E. Fradkin, Critical behavior of disordered degenerate semiconductors. I. Models, symmetries, and formalism, Phys. Rev. B **33**, 3257 (1986).

[4] F. D. M. Haldane, Model for a quantum Hall effect without Landau levels: Condensed-matter realization of the "parity anomaly," Phys. Rev. Lett. **61**, 2015 (1988).

[5] P. A. Lee, Localized states in a d-wave superconductor, Phys. Rev. Lett. **71**, 1887 (1993).

[6] M. V. Berry and R. J. Mondragon, Neutrino billiards: Time-reversal symmetry-breaking without magnetic fields, Proc. R. Soc. London, Ser. A **412**, 53 (1987).

[7] K. S. Novoselov, A. K. Geim, S. V. Morozov, D.-e. Jiang, Y. Zhang, S. V. Dubonos, I. V. Grigorieva, and A. A. Firsov, Electric field effect in atomically thin carbon films, Science **306**, 666 (2004).

[8] A. H. Castro Neto, F. Guinea, N. M. R. Peres, K. S. Novoselov, and A. K. Geim, The electronic properties of graphene, Rev. Mod. Phys. **81**, 109 (2009).

[9] M. Z. Hasan and C. L. Kane, Colloquium: Topological insulators, Rev. Mod. Phys. **82**, 3045 (2010).

[10] S. Das Sarma, S. Adam, E. H. Hwang, and E. Rossi, Electronic transport in two-dimensional graphene, Rev. Mod. Phys. **83**, 407 (2011).

[11] X.-L. Qi and S.-C. Zhang, Topological insulators and superconductors, Rev. Mod. Phys. **83**, 1057 (2011).

[12] S. Manzeli, D. Ovchinnikov, D. Pasquier, O. V. Yazyev, and A. Kis, 2D transition metal dichalcogenides, Nat. Rev. Mater. **2**, 17033 (2017).

[13] A. K. Geim and K. S. Novoselov, The rise of graphene, Nat. Mater. **6**, 183 (2007).

[14] N. H. Shon and T. Ando, Quantum transport in two-dimensional graphite system, J. Phys. Soc. Jpn. **67**, 2421 (1998).

[15] J. Tworzydło, B. Trauzettel, M. Titov, A. Rycerz, and C. W. J. Beenakker, Sub-Poissonian shot noise in graphene, Phys. Rev. Lett. **96**, 246802 (2006).

[16] F. Miao, S. Wijeratne, Y. Zhang, U. Coskun, W. Bao, and C. Lau, Phase-coherent transport in graphene quantum billiards, Science **317**, 1530 (2007).

[17] T. Ando, Y. Zheng, and H. Suzuura, Dynamical conductivity and zero-mode anomaly in honeycomb lattices, J. Phys. Soc. Jpn. **71**, 1318 (2002).

[18] P. M. Ostrovsky, I. V. Gornyi, and A. D. Mirlin, Electron transport in disordered graphene, Phys. Rev. B **74**, 235443 (2006).

[19] E. G. Mishchenko, Effect of electron-electron interactions on the conductivity of clean graphene, Phys. Rev. Lett. **98**, 216801 (2007).

[20] I. F. Herbut, V. Juričić, and O. Vafek, Coulomb interaction, ripples, and the minimal conductivity of graphene, Phys. Rev. Lett. **100**, 046403 (2008).

[21] B. Rosenstein, M. Lewkowicz, and T. Maniv, Chiral anomaly and strength of the electron-electron interaction in graphene, Phys. Rev. Lett. **110**, 066602 (2013).

[22] A. D. Güçlü, P. Potasz, M. Korkusinski, P. Hawrylak *et al.*, *Graphene Quantum Dots* (Springer, New York, 2014).

[23] M. Zarenia, A. Chaves, G. A. Farias, and F. M. Peeters, Energy levels of triangular and hexagonal graphene quantum dots: A comparative study between the tight-binding and Dirac equation approach, Phys. Rev. B **84**, 245403 (2011).

[24] T. Yamamoto, T. Noguchi, and K. Watanabe, Edge-state signature in optical absorption of nanographenes: Tight-binding method and time-dependent density functional theory calculations, Phys. Rev. B **74**, 121409(R) (2006).

[25] I. Ozfidan, M. Korkusinski, A. D. Güçlü, J. A. McGuire, and P. Hawrylak, Microscopic theory of the optical properties of colloidal graphene quantum dots, Phys. Rev. B **89**, 085310 (2014).

[26] Z. Fang, Y. Wang, A. E. Schlather, Z. Liu, P. M. Ajayan, F. J. García de Abajo, P. Nordlander, X. Zhu, and N. J. Halas, Active tunable absorption enhancement with graphene nanodisk arrays, Nano Lett. **14**, 299 (2014).

[27] R. Pohle, E. G. Kavousanaki, K. M. Dani, and N. Shannon, Symmetry and optical selection rules in graphene quantum dots, Phys. Rev. B **97**, 115404 (2018).

[28] J. Lu, P. S. E. Yeo, C. K. Gan, P. Wu, and K. P. Loh, Transforming C60 molecules into graphene quantum dots, Nat. Nanotechnol. **6**, 247 (2011).

[29] N. Mohanty, D. Moore, Z. Xu, T. Sreeprasad, A. Nagaraja, A. A. Rodriguez, and V. Berry, Nanotomy-based production of transferable and dispersible graphene nanostructures of controlled shape and size, Nat. Commun. **3**, 844 (2012).

[30] M. Olle, G. Ceballos, D. Serrate, and P. Gambardella, Yield and shape selection of graphene nanoislands grown on Ni (111), Nano Lett. **12**, 4431 (2012).

[31] K. A. Ritter and J. W. Lyding, The influence of edge structure on the electronic properties of graphene quantum dots and nanoribbons, Nat. Mater. **8**, 235 (2009).

[32] S. Zhu, J. Zhang, C. Qiao, S. Tang, Y. Li, W. Yuan, B. Li, L. Tian, F. Liu, R. Hu *et al.*, Strongly green-photoluminescent graphene quantum dots for bioimaging applications, Chem. Commun. **47**, 6858 (2011).

[33] M. R. Younis, G. He, J. Lin, and P. Huang, Recent advances on graphene quantum dots for bioimaging applications, Front. Chem. **8**, 424 (2020).

[34] Y. Li, Y. Hu, Y. Zhao, G. Shi, L. Deng, Y. Hou, and L. Qu, An electrochemical avenue to green-luminescent graphene quantum dots as potential electron-acceptors for photovoltaics, Adv. Mater. **23**, 776 (2011).

[35] B. Trauzettel, D. V. Bulaev, D. Loss, and G. Burkard, Spin qubits in graphene quantum dots, Nat. Phys. **3**, 192 (2007).

[36] C. O. Kim, S. W. Hwang, S. Kim, D. H. Shin, S. S. Kang, J. M. Kim, C. W. Jang, J. H. Kim, K. W. Lee, S.-H. Choi *et al.*, High-performance graphene-quantum-dot photodetectors, Sci. Rep. **4**, 5603 (2014).

[37] Y. Zhai, B. Zhang, R. Shi, S. Zhang, Y. Liu, B. Wang, K. Zhang, G. I. Waterhouse, T. Zhang, and S. Lu, Carbon dots as new building blocks for electrochemical energy storage and electrocatalysis, Adv. Energy Mater. **12**, 2103426 (2022).

[38] M. Li, T. Chen, J. J. Gooding, and J. Liu, Review of carbon and graphene quantum dots for sensing, ACS Sens. **4**, 1732 (2019).

[39] S. L. Ting, S. J. Ee, A. Ananthanarayanan, K. C. Leong, and P. Chen, Graphene quantum dots functionalized gold nanoparticles for sensitive electrochemical detection of heavy metal ions, Electrochim. Acta **172**, 7 (2015).

[40] H. K. Avetissian, *Relativistic Nonlinear Electrodynamics: The QED Vacuum and Matter in Super-Strong Radiation Fields* (Springer, New York, 2015), Vol. 88.

[41] P. B. Corkum, Plasma perspective on strong field multiphoton ionization, Phys. Rev. Lett. **71**, 1994 (1993).

[42] G. P. Zhang, Optical high harmonic generation in C 60, Phys. Rev. Lett. **95**, 047401 (2005).

[43] G. P. Zhang and T. F. George, Ellipticity dependence of optical harmonic generation in C 60, Phys. Rev. A **74**, 023811 (2006).

[44] G. P. Zhang and Y. H. Bai, High-order harmonic generation in solid C 60, Phys. Rev. B **101**, 081412(R) (2020).

[45] H. K. Avetissian, A. G. Ghazaryan, and G. F. Mkrtchian, High harmonic generation in fullerene molecules, Phys. Rev. B **104**, 125436 (2021).

[46] H. K. Avetissian, S. Sukiasyan, H. H. Matevosyan, and G. F. Mkrtchian, Disorder-induced effects in high-harmonic generation process in fullerene molecules, Results Phys. **53**, 106951 (2023).

[47] J. D. Cox, A. Marini, and F. J. G. De Abajo, Plasmon-assisted high-harmonic generation in graphene, Nat. Commun. **8**, 14380 (2017).

[48] H. K. Avetissian, B. R. Avchyan, G. F. Mkrtchian, and K. A. Sargsyan, On the extreme nonlinear optics of graphene nanoribbons in the strong coherent radiation fields, J. Nanophotonics **14**, 026018 (2020).

[49] X. Zhang, T. Zhu, H. Du, H.-G. Luo, J. van den Brink, and R. Ray, Extended high-harmonic spectra through a cascade resonance in confined quantum systems, Phys. Rev. Res. **4**, 033026 (2022).

[50] B. Avchyan, A. Ghazaryan, K. Sargsyan, and K. V. Sedrakian, High harmonic generation in triangular graphene quantum dots, J. Exp. Theor. Phys. **134**, 125 (2022).

[51] B. R. Avchyan, A. G. Ghazaryan, S. S. Israelyan, and K. V. Sedrakian, High harmonic generation with many-body Coulomb interaction in rectangular graphene quantum dots of armchair edge, J. Nanophoton. **16**, 036001 (2022).

[52] B. Avchyan, A. Ghazaryan, K. Sargsyan, and K. V. Sedrakian, On laser-induced high-order wave mixing and harmonic generation in a graphene quantum dot, JETP Lett. **116**, 428 (2022).

[53] S. Gnawali, R. Ghimire, K. R. Magar, S. J. Hossaini, and V. Apalkov, Ultrafast electron dynamics of graphene quantum dots: High harmonic generation, Phys. Rev. B **106**, 075149 (2022).

[54] H. K. Avetissian, A. G. Ghazaryan, K. V. Sedrakian, and G. F. Mkrtchian, Long-range correlation-induced effects at high-order harmonic generation on graphene quantum dots, Phys. Rev. B **108**, 165410 (2023).

[55] V. M. Pereira, F. Guinea, J. M. B. Lopes dos Santos, N. M. R. Peres, and A. H. Castro Neto, Disorder induced localized states in graphene, Phys. Rev. Lett. **96**, 036801 (2006).

[56] J. J. Palacios, J. Fernández-Rossier, and L. Brey, Vacancy-induced magnetism in graphene and graphene ribbons, Phys. Rev. B **77**, 195428 (2008).

[57] R. Nair, M. Sepioni, I.-L. Tsai, O. Lehtinen, J. Keinonen, A. V. Krasheninnikov, T. Thomson, A. Geim, and I. Grigorieva, Spin-half paramagnetism in graphene induced by point defects, Nat. Phys. **8**, 199 (2012).

[58] K.-i. Sasaki, Y. Kawazoe, and R. Saito, Local energy gap in deformed carbon nanotubes, Prog. Theor. Phys. **113**, 463 (2005).

[59] S. V. Morozov, K. S. Novoselov, M. I. Katsnelson, F. Schedin, L. A. Ponomarenko, D. Jiang, and A. K. Geim, Strong suppression of weak localization in graphene, Phys. Rev. Lett. **97**, 016801 (2006).

[60] A. F. Morpurgo and F. Guinea, Intervalley scattering, long-range disorder, and effective time-reversal symmetry breaking in graphene, Phys. Rev. Lett. **97**, 196804 (2006).

[61] F. Guinea, M. I. Katsnelson, and A. Geim, Energy gaps and a zero-field quantum Hall effect in graphene by strain engineering, Nat. Phys. **6**, 30 (2010).

[62] N. Levy, S. Burke, K. Meaker, M. Panlasigui, A. Zettl, F. Guinea, A. C. Neto, and M. F. Crommie, Strain-induced pseudo–magnetic fields greater than 300 tesla in graphene nanobubbles, Science **329**, 544 (2010).

[63] E. Goulielmakis and T. Brabec, High harmonic generation in condensed matter, Nat. Photon. **16**, 411 (2022).

[64] L. Yue and M. B. Gaarde, Introduction to theory of high-harmonic generation in solids: Tutorial, J. Opt. Soc. Am. B **39**, 535 (2022).

[65] H. Koochaki Kelardeh, V. Apalkov, and M. I. Stockman, Graphene superlattices in strong circularly polarized fields: Chirality, Berry phase, and attosecond dynamics, Phys. Rev. B **96**, 075409 (2017).

[66] D. Bauer and K. K. Hansen, High-harmonic generation in solids with and without topological edge states, Phys. Rev. Lett. **120**, 177401 (2018).

[67] R. Silva, Á. Jiménez-Galán, B. Amorim, O. Smirnova, and M. Ivanov, Topological strong-field physics on sub-laser-cycle timescale, Nat. Photon. **13**, 849 (2019).

[68] C. Heide, Y. Kobayashi, D. R. Baykusheva, D. Jain, J. A. Sobota, M. Hashimoto, P. S. Kirchmann, S. Oh, T. F. Heinz, D. A. Reis *et al.*, Probing topological phase transitions using high-harmonic generation, Nat. Photon. **16**, 620 (2022).

[69] T. T. Luu and H. J. Wörner, Measurement of the Berry curvature of solids using high-harmonic spectroscopy, Nat. Commun. **9**, 916 (2018).

[70] L. Yue and M. B. Gaarde, Characterizing anomalous high-harmonic generation in solids, Phys. Rev. Lett. **130**, 166903 (2023).

[71] C. Yu, K. K. Hansen, and L. B. Madsen, Enhanced high-order harmonic generation in donor-doped band-gap materials, Phys. Rev. A **99**, 013435 (2019).

[72] C. Yu, K. K. Hansen, and L. B. Madsen, High-order harmonic generation in imperfect crystals, Phys. Rev. A **99**, 063408 (2019).

[73] A. Pattanayak, M. S. Mrudul, and G. Dixit, Influence of vacancy defects in solid high-order harmonic generation, Phys. Rev. A **101**, 013404 (2020).

[74] T. Hansen and L. B. Madsen, Doping effects in high-harmonic generation from correlated systems, Phys. Rev. B **106**, 235142 (2022).

[75] A. Goft, Y. Abulafia, N. Orion, C. L. Schochet, and E. Akkermans, Defects in graphene: A topological description, Phys. Rev. B **108**, 054101 (2023).

[76] O. Ovdat, Y. Don, and E. Akkermans, Vacancies in graphene: Dirac physics and fractional vacuum charges, Phys. Rev. B **102**, 075109 (2020).

[77] L. Linhart, J. Burgdorfer, and F. Libisch, Accurate modeling of defects in graphene transport calculations, Phys. Rev. B **97**, 035430 (2018).

[78] P. Potasz, A. D. Güçlü, and P. Hawrylak, Spin and electronic correlations in gated graphene quantum rings, Phys. Rev. B **82**, 075425 (2010).

[79] A. L. C. Pereira and P. A. Schulz, Additional levels between Landau bands due to vacancies in graphene: Towards defect engineering, Phys. Rev. B **78**, 125402 (2008).

[80] F. Ding, Theoretical study of the stability of defects in single-walled carbon nanotubes as a function of their distance from the nanotube end, Phys. Rev. B **72**, 245409 (2005).

[81] V. M. Pereira, J. M. B. Lopes dos Santos, and A. H. Castro Neto, Modeling disorder in graphene, Phys. Rev. B **77**, 115109 (2008).

[82] G.-D. Lee, C. Z. Wang, E. Yoon, N.-M. Hwang, D.-Y. Kim, and K. M. Ho, Diffusion, coalescence, and reconstruction of vacancy defects in graphene layers, Phys. Rev. Lett. **95**, 205501 (2005).

[83] B. Kramer and A. MacKinnon, Localization: Theory and experiment, Rep. Prog. Phys. **56**, 1469 (1993).

[84] S. Nandy and I. Sodemann, Symmetry and quantum kinetics of the nonlinear Hall effect, Phys. Rev. B **100**, 195117 (2019).

[85] T. Stauber, N. M. R. Peres, and A. K. Geim, Optical conductivity of graphene in the visible region of the spectrum, Phys. Rev. B **78**, 085432 (2008).

[86] T. Morimoto, Y. Hatsugai, and H. Aoki, Optical Hall conductivity in 2DEG and graphene QHE systems, Physica E **42**, 751 (2010).

[87] A. Ferreira, J. Viana-Gomes, Y. V. Bludov, V. Pereira, N. M. R. Peres, and A. H. Castro Neto, Faraday effect in graphene enclosed in an optical cavity and the equation of motion method for the study of magneto-optical transport in solids, Phys. Rev. B **84**, 235410 (2011).

[88] C.-Z. Chang, C.-X. Liu, and A. H. MacDonald, Colloquium: Quantum anomalous Hall effect, Rev. Mod. Phys. **95**, 011002 (2023).

[89] G. P. Zhang, M. S. Si, M. Murakami, Y. H. Bai, and T. F. George, Generating high-order optical and spin harmonics from ferromagnetic monolayers, Nat. Commun. **9**, 3031 (2018).

[90] H. K. Avetissian, V. N. Avetisyan, B. R. Avchyan, and G. F. Mkrtchian, High-order harmonic generation in three-dimensional Weyl semimetals with broken time-reversal symmetry, Phys. Rev. A **106**, 033107 (2022).

[91] X.-M. Tong and Shih-I. Chu, Probing the spectral and temporal structures of high-order harmonic generation in intense laser pulses, Phys. Rev. A **61**, 021802(R) (2000).

[92] J. Mao, Y. Jiang, D. Moldovan, G. Li, K. Watanabe, T. Taniguchi, M. R. Masir, F. M. Peeters, and E. Y. Andrei, Realization of a tunable artificial atom at a supercritically charged vacancy in graphene, Nat. Phys. **12**, 545 (2016).

[93] O. Ovdat, J. Mao, Y. Jiang, E. Andrei, and E. Akkermans, Observing a scale anomaly and a universal quantum phase transition in graphene, Nat. Commun. **8**, 507 (2017).